Reconfigurable photonic integrated circuits (RPICs) based on functional materials for integrated optical communication applications

Faneca, Joaquin, Dominguez Bucio, Thalia, Gardes, Frederic, Baldycheva, Anna

Reconfigurable photonic integrated circuits (RPICs) based on functional materials for integrated optical communication applications

Joaquin Faneca[1,2], Thalia Dominguez Bucio[2], Frederic Y. Gardes[2], and Anna Baldycheva[1]

[1] Department of Engineering, University of Exeter, EX4 4QF, UK
[2] Optoelectronics Research Centre, Building 53, University of Southampton, SO17 1BJ, UK

ABSTRACT

In this work we combine the already mature silicon and silicon nitride platforms with novel reconfigurable materials such as 2D materials, liquid crystals and phase change materials. An actively reconfigurable 1D photonic crystal multi-channel filter based on Si-on-insulator and liquid crystal platforms is demonstrated with extraordinary large quality factor, $Q \sim 10^4$. A complete study and design of an optical routing and multilevel volatile photonic memory based on graphene capacitor concept for future high performance computing using Silicon rich nitride is shown with a bandwidth of 64 GHz and energy power consumption per bit as low as 0.22 pJ. Finally, an optical switch based on germanium-antimony-tellurium phase change material (GST) is experimentally demonstrated for O-band operation with the extinction ratio as high as 10 dB between the amorphous and the crystalline states.

Keywords: Silicon Photonics, Functional materials, Tunable devices, Reconfigurable Integrated Circuits

1. INTRODUCTION

1.1 Silicon Photonics

During the last 20 years, the silicon photonics technology has emerged as a powerful material to create photonic devices. Companies like Lumentum, Intel, Rockley Photonics, IBM and Hewlett-Packard are focused on silicon photonics as the future technology for the high-speed data processing as demonstrated by the first products on the market.[1] Furthermore, silicon photonics scientific community has developed process flows that allow effective use of the CMOS fabrication infrastructure to build complex photonic circuits, where the information can be transferred from electronic to optical domain and back again.[2] The wafers that are commonly used in silicon photonics are "silicon on insulator". The typical size is 12" wafer which consists of a 725 μm silicon substrate, 2 μm of oxide (buried oxide, or BOX) and 220 nm of crystalline silicon. For applications in the visible range or in the mid-infrared, silicon is not a useful material due to its strong absorbent properties, however, silicon nitride (Si_3N_4) shows far less absorbency in these ranges of the spectrum while retaining similar properties and material interactions to those seen for silicon in the near infrared regime of the spectrum.[3,4] The waveguides structures and photonic circuits are patterns within the crystalline silicon or silicon nitride wafers, consequently, the material properties of silicon and silicon nitride are important for the device design. Si_3N_4 optical properties allow less confinement of the mode within the photonic circuits components, improving the interaction with the materials that can be deposited on the top of the passive structures and avoiding the two photon absorption problem in silicon,[5] however, the footprint of the devices is larger than in silicon due to the bending losses of the structures and the mode confinement.[6]

Silicon Photonics is now established as a mature technology for different applications such as biosensing,[7] optical communications applications,[1] high performance computing (HPC),[8] quantum computing,[9] etc. Silicon and silicon nitride photonic integrated circuits (PICs) have been demonstrated by different devices such as: modulators,[10–16] photodetectors,[17] switchers,[18] memories.[19] A range of volatile[20] and non-volatile[21] reconfigurable

---

Further author information: (Send correspondence to Joaquin Faneca.)
Joaquin Faneca: E-mail: jf481@exeter.ac.uk

photonic integrated circuits have been already demonstrated using key components such as integrated optical modulators. These modulators are based on the plasma dispersion effect,[22] quantum confined Stark effect[23] or Frantz Keldysh effect.[24] These processes are usually non-cost effective as they require tens of fabrication steps and are only available for silicon and germanium based waveguides . Over the last 10 years, a substantial effort has been pursued in terms of the simplification of fabrication processes by looking at novel reconfigurable technologies for PIC providing equivalent or better performance compared to group IV based materials. Ideal candidates are: liquid crystals, graphene enabled modulators or photodetectors, and optical phase change materials, which can easily be integrated to most passive photonic integrated circuits (PICs).

1.2 Functional Materials

1.2.1 Liquid crystals (LC)

A liquid crystal is a state of matter which is liquid-like and crystalline at the same time. Crystalline mesophases possess some typical properties of a liquid, such as fluidity and the inability to support shear, formation and coalescence of droplets. These mesophases also have certain crystalline properties, such as anisotropy of optical, electrical, and magnetic properties, as well as a periodic arrangement of molecules in one or more spatial directions. Depending on the arrangement of the molecules in a mesophase, liquid crystals are subdivided into nematics, smectics and cholesterics[25] [Fig. 1].

- **Nematic liquid crystal**: In a nematic mesophase molecules possess a long-range orientational order with molecular long axes aligned along a preferred direction. The preferred direction may vary throughout the medium and is called a director. The orientation of the director is represented by a unit vector, $\mathbf{d(r)}$. In a nematic, the molecules are able to rotate around their long axes, and there is no preferential arrangement of their ends, even if they differ [Fig. 1(a)].

- **Smectic liquid crystal**: The important feature of a smectic mesophase, which distinguishes it from a nematic or a cholesteric one, is its stratification.The molecules are arranged in layers and exhibit some correlations in their positions in addition to the orientational ordering. The layers can slide freely over one another. Depending on the molecular order in layers, a number of different types of smectics have been observed. In a smectic, molecules are aligned perpendicular to the layers, without long-range crystalline ordering within them [Fig. 1(b)].

- **Cholesteric liquid crystal**: In a cholesteric mesophase the average molecular orientation twists through the medium with a certain periodicity, p. The cholesteric mesophase is similar to the nematic, it has a long-range orientational order, but no long-range positional order of the centers of mass of molecules. It differs from the nematic mesophase in the sense that the director varies throughout the medium in a regular way even in an unstrained state. The director distribution is precisely what would be obtained by twisting a nematic aligned along the y axis around the x axis. In any plane perpendicular to the twist axis the long axes of the molecules align along a single preferred direction in this plane, but in a series of parallel planes this direction rotates uniformly [Fig. 1 (c)].

The liquid crystals used to make electro-optic devices are usually of sufficiently high resistivity, hence they can be treated as ideal dielectric materials. Because of the elongated shape of the constituent molecules, and their ordered orientation, liquid crystals have anisotropic dielectric properties with uniaxial symmetry. The dielectric permittivity is $\varepsilon_{||}$ for electric fields pointing in the direction of the molecules and $\varepsilon_{\perp}$ in the perpendicular direction. Liquid crystals for which $\varepsilon_{||} > \varepsilon_{\perp}$ (positive uniaxial) are usually selected for electro-optic applications. When a steady electric field is applied, electric dipoles are induced and the resultant electric forces exert torques on the molecules. The molecules rotate in a direction such that the free electrostatic energy, $-1/2\mathbf{E} \cdot \mathbf{D} = -1/2 \left[\varepsilon_{\perp} E_1^2 + \varepsilon_{\perp} E_2^2 + \varepsilon_{||} E_3^2 \right]$, is minimized. The electric field components are in the direction of the principal axes, due to the positive uniaxial condition. For a given direction of the electric field, minimum energy is achieved, when the molecules are aligned with the field, so $E_1 = E_2 = 0$ and $\mathbf{E} = (0, 0, E)$, and the energy is then $-1/2 \cdot \varepsilon_{||} E^2$. If an electric field is generated by applying a voltage across transparent conductive electrodes coated on the inside of the glass plates, the resultant electric forces tend to tilt the molecules toward alignment
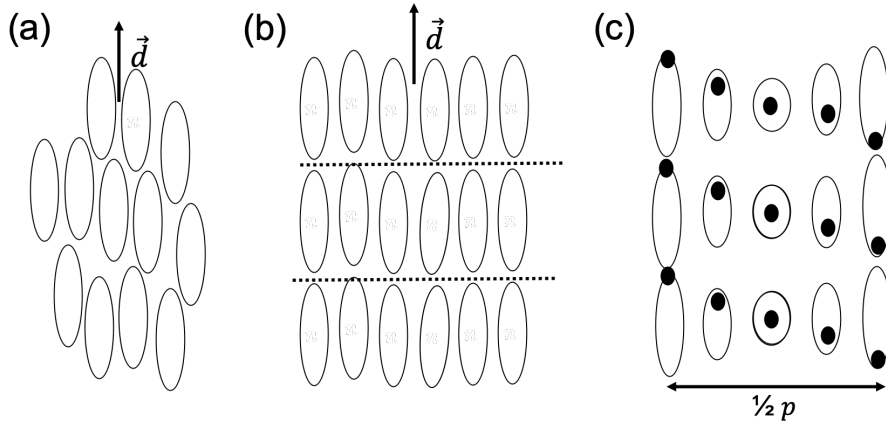
Figure 1. (a) Nematic liquid crystal (b) Smectic liquid crystal (c) Cholesteric liquid crystal

with the field, but the elastic forces at the surfaces of the glass plates resist this motion. The equilibrium tilt angle θ for most molecules is a monotonically increasing function of voltage (V) and can be described as:

$$\theta = \begin{cases} 0, & V < V_c \\ \pi/2 - 2 \cdot \tanh\left[e^{-\frac{V-V_c}{V_0}}\right], & V > V_c \end{cases} \tag{1}$$

where V is the applied voltage, V_c is the critical voltage at which the tilting process begins, and V_0 is the constant. When $V - V_c = V_0$, $\theta \approx 50°$, as $V - V_c$ increases beyond V_0, θ approaches $90°$. When the electric field is removed, the orientation of the molecules near the glass plates is reasserted and all of the molecules tilt back to their original orientations, in planes parallel to the plates. The liquid crystal refractive index angle dependence can be described by:

$$n_c(\theta) = \frac{n_o n_e}{\sqrt{n_o^2 \sin^2(\theta) + n_e^2 \cos^2(\theta)}} \tag{2}$$

where n_o and n_e are the ordinary and extraordinary refractive indexes respectively. In a sense, the liquid-crystal material may be viewed as a liquid with memory. Different reconfigurable photonic integrated circuits can be designed and fabricated exploiting the tunability of the liquid crystal refractive index.

1.2.2 2D materials

Nowadays, the term of 2D materials is applied to a crystalline material which consist of a single or a few layers of atoms, with a thickness varying from one atomic layer to more than ten nanometres.[26] Owing to their atomic layer thickness, strong light-matter interaction, high non-linearity, broadband optical response, fast tunablility, controllable optoelectronic properties, and high compatibility with other photonic structures, 2D materials, including graphene, transition metal dichalcogenides and black phosphorus, have been attracting increasing attention for photonic integrated applications.[27–31] By fine tuning of the density of carriers by electric field effect or optical effect, a tune in the physical properties can be achieved (e.g Fermi level or nonlinear absorption). Consequently, the refractive index of the 2D materials can be instantly changed, making them versatile for different reconfigurable PICs applications in optical communications.

- **Graphene:** Graphene is a single layer of a graphite crystal. It consists of a single atomic layer of pure covalently bonded carbon atoms arranged in a two-dimensional hexagonal lattice structure. Each carbon atom has six electrons surrounding its nucleus, two in the inner shell and four in the outer electron shell. Three out of these four electrons are bound with the nearest-neighbour atoms electrons and creates the strong chemical bonds that makes graphene one of the strongest materials, whereas the other electron in

the outer electron shell of each carbon atom is delocalized in the entire graphene layer.[32] The energy band structure of the delocalized electron determines graphene's conductivity. While in non-conducting or semiconducting materials the full valence band and the empty conduction band are separated by an energy gap, there is no gap between the conduction and valence bands in pure graphene. Thus, pure graphene can be regarded as a zero-gap semiconductor. Similarly, while in metals the valence band is partially filled, in pure graphene the Fermi level lies at the point where the conduction and valence bands meet (the Dirac point).[33]

The duality between semiconductor and metallic behaviour can be controlled by tuning the position of the Fermi level from the Dirac point, either by chemical additions, or, more easily, by using the electric field effect applying a constant voltage (gating the graphene) between a graphene and a metallic layer or a graphene capacitor, separated by a very thin insulator, thus the resulting electrical field modifies the quantity of conduction carriers and consequently graphene's electrical conductivity. For a given polarity of the voltage, that is, for a given direction of the DC electric field, the conduction band fills up, which means that electrons are added to the system. For the other polarity, the number of electrons in the valence band is reduced, which means that holes are added to the system [Fig. 2].
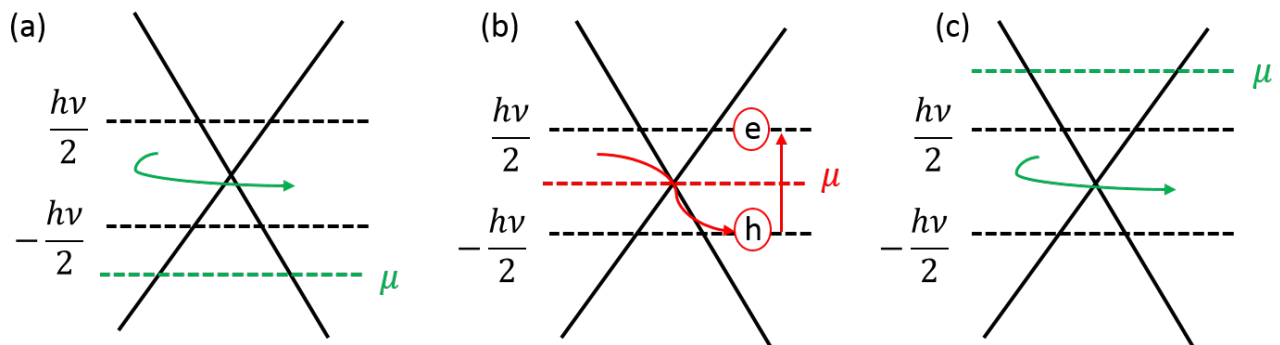

Figure 2. Schematic of a graphene band diagram gated when (a) The Fermi level is under the valence band and no absorption occurs since both, the valence and the conduction bands are empty. (b) Absorption takes place when the Fermi level is between the valence and conduction bands generating electron-hole pairs and (c) Fermi level is above the conduction band and no absorption occurs due to the full valence and conduction bands.

The unique opto-electronic behavior of graphene is due to both its two-dimensional (2D) structure that confines electrons in one atomic layer and its low density of states (DOS) near the Dirac point, which causes the Fermi energy (E_F) to shift significantly with variation of carrier density.[34] For example, a Fermi level up to 0.9 eV has been experimentally demonstrated using the electrostatic field gating technique.[35] The tunable band-gap of graphene offers great opportunities and flexibility for infrared and visible light manipulation on chip.

- **Transition Metal Dichalcogenides (TMDs):** 2D TMDs are atomically thin semiconductors of the type MX_2, where **M** is a transition metal atom and **X** is a chalcogen atom. Typically, TMDs have bandgaps ranging from 1 to 2.5 eV, corresponding to near-infrared and visible frequencies. The band gap of bulk TMD material down to a thickness of two monolayers is still indirect, so the emission efficiency is lower compared to monolayered materials. The emission efficiency is about 10^4 greater for TMD monolayer than for bulk materials.[36] The band gaps of TMD monolayers are in the visible range (between 400 nm and 700 nm). Owing to their direct band gap, TMD monolayers are promising materials for optoelectronics applications as emitters on chip. Two of the most used and promising TMDs materials are MoS_2 and WS_2[37] which maintain some of the outstanding properties of graphene[38][Fig. 3].
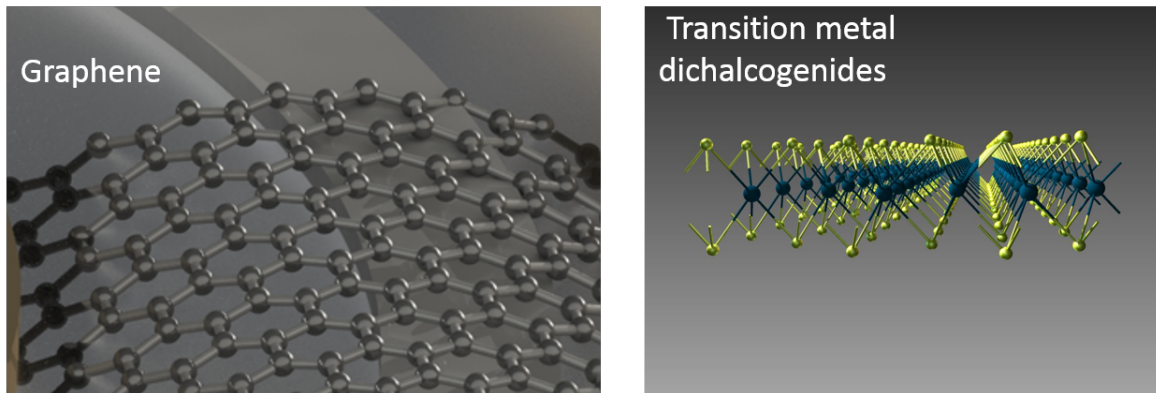
Figure 3. Intrinsic single-layer graphene is a zero-bandgap semimetallic material while its Fermi level can be tuned up to 1 eV under external electric field, covering the range from THz to visible wavelength. The transition metal dichalcogenides have layer number-dependent bandgaps ranging from 1.0 to 2.5 eV[26] .

1.3 Phase change materials (PCMs)

Phase change materials are characterized by a unique optoelectronic property. They possess a pronounced difference of optical and electronic properties depending upon their atomic arrangement, i.e. whether they are amorphous or crystalline. At the same time they can be rapidly switched between the amorphous and crystalline state. This combination of properties is attractive for various optoelectronic applications. This technology initially found applications in optical disks (CDs, DVDs), due to significant advantages over other existed technologies, such as the fast write time for changing the state, relatively high potential data density, and ability to be rewritable.[39–43] The phase change process can be thermally,[44] optically[45] or electrically[46] driven, and can be sub-nanosecond depending on the specific alloy.[47,48] Crystallization is achieved by heating the material above the glass transition temperature and then slowly cooling it down. Typically, the thermal excitation is achieved using a laser pulse, but can also be provided electrostatically or by any other method by which heat can be transferred to the sample. The phase change can be either a liquid-solid change or a solid-solid change where the molecular structure is reconfigured from an amorphous state to an ordered crystalline state and most importantly it is a reversible process[21] [Fig. 4]. In rewriteable optical data storage employing phase change materials a short pulse of a focused, high intensity laser beam locally heats the phase change material above its melting temperature. Rapidly cooling the phase change alloy with rates higher than 10^9K/s quenches the liquid-like state into a disordered, amorphous phase. This amorphous state has different optical properties than the surrounding crystalline state. Hence detecting regions with amorphous structure is straightforward employing a laser beam of low intensity. To erase the stored information a laser pulse with intermediate power is utilized. The laser locally heats the phase change film above the crystallization temperature. At elevated temperatures above the glass transition temperature the atoms become increasingly mobile and can revert to the energetically favourable crystalline state, erasing the recorded information. In electronic memory applications of phase change materials a short and relatively high current pulse is used to locally melt the crystalline material. The resulting amorphous state has a high resistance which exceeds the resistance of the crystalline state by several orders of magnitude ($10^2 - 10^3$).[49] An intermediate power pulse is used to heat the material above its crystallization temperature to switch it back to the crystalline, low resistance state, while a low power pulse is used to determine the resistance of the phase change material. Different phase change materials have been developed where the temperature required to change the phase as desired can span a large range of possible values.[50] On changing the phase of the material, the refractive index for the material is altered, the tunability of the refractive index gives rise to potential applications in reconfigurable photonic integrated circuits.
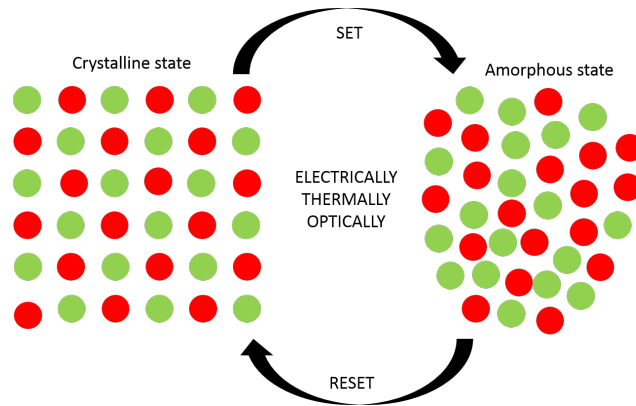
Figure 4. Phase change material working principle. The PCM can be switched between states, optically, thermally or electrically, when switch occurs from crystalline to amorphous (SET) or when switch occurs from amorphous to crystalline (RESET)

2. RESULTS AND DISCUSSION

2.1 1D Photonic crystal based on liquid crystals

We have theoretically and experimentally demonstrated a Fabry-Pérot (FP) resonators based on a Si-air one-dimensional photonic crystal (1D PhC) with coupled triple-cavity modes (or defects).[51] These defects are obtained by filling selected air channels in the 1D PhC with an actively reconfigurable fluid [Fig. 5 (a)]. Simulations of the optical properties of these FP resonators were performed in the wide infrared spectral range. It is shown that by changing the refractive index, n_c, of the fluid simultaneously in all three channels, a set of narrow triple resonance peaks can be obtained within wide stop-bands of different order in the infrared range [Fig. 6 (a)]. In addition, at certain values of the central cavity n_c, splitting of the triple resonance peaks into a single peak with a significantly larger quality factor, $Q = 21,200$, occurs [Fig. 6 (b)]. Prototype devices based on Silicon-On-Insulator platform were fabricated and characterized by electro-optical and spectroscopic measurements. The electro-optical measurements demonstrate the possibility of refractive index manipulation of the filler in the FP cavities individually or simultaneously. Spectroscopic measurements performed in the range 1540–1630 nm using fiber-coupling confirm the presence of triple resonance peaks in the 3rd stop-band in the absence of an electric field applied to the FP channels. At an applied voltage of 10 V to the middle cavity, an increase of Q to 3720 in the single peak is registered.[52]
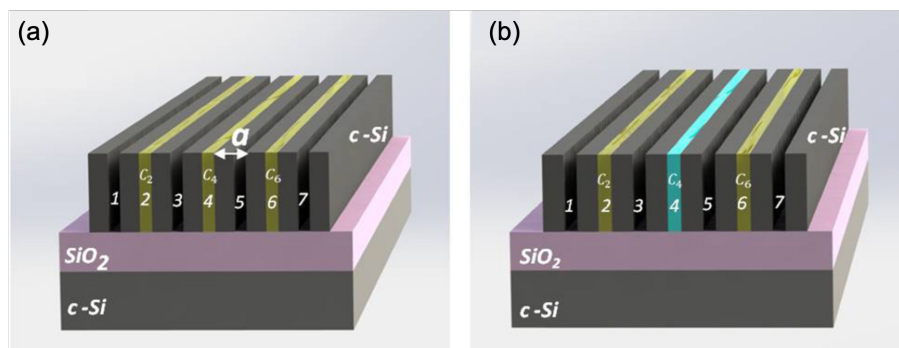

Figure 5. (a) Schematic diagram of 1D PhC based on a Si-air structure with three central air cavities (c_2, c_4, and c_6) infiltrated with a nematic liquid crystal (LC) of tunable refractive index, n_c. (b) Schematic diagram of 1D PhC in which the refractive index of the central cavity n_{c4} is changed without changing n_c in the edge cavities, giving a new sequence of n_c. The notation (a) stands for the lattice constant of the 1D PhC and is equal to a sum of the thicknesses of crystalline Si (c-Si) rib, d_{Si}, and the air (or LC) cavity, d_{air}.[51]

The device was electrically driven by terminating probes on the contact pads during the transmission measurements using a customized Microtech 2 probe coupler. Device transmission characteristics were initially assessed

with no voltage applied to the channels. In Fig. 6(a) we demonstrate the realization of a triple resonance mode obtained with a spontaneously aligned LC in the grooves with an average refractive index of 1.68. The simulated resonance peaks obtained at 1,589.4, 1,608 and 1,629.6 nm demonstrate a Q factor of the order of 1,130 with a total resonance wavelength spacing of 40.2 nm. Under an applied AC voltage of 10V, the refractive index of c_4 channel is decreased to 1.458. This results in the formation of a doublet at 1,607.6 and 1,617 nm and a single resonance peak at 1,562.4 nm, with a significant increase of the Q factor to 3,720, see Fig. 6(b). Under applied voltage, this peak is shifted by 27 nm from its original position at 1,589.4 nm, as shown in Fig. 6(a) with no voltage applied. The fitted n_c value corresponds to a homeotropic alignment of rod-like LC molecules perpendicular to the Si walls, expected to occur with an applied electric field across the 1D PhC groove channels. This experimental result demonstrates for the first time, electrically controllable, ultrahigh sensitivity of a single resonance device based on the triple cavity Fabry-Pérot system. The LC filler in the 2nd and 6th cavities can be replaced by any other liquid filler analyse or gas with arbitrary refractive index, while the electrically tunable 4th central cavity can be used as a highly-sensitive reference liquid. The nematic LC E7 can demonstrate a relatively high-quality factor and sensitivity for high-order stop-bands in particular.
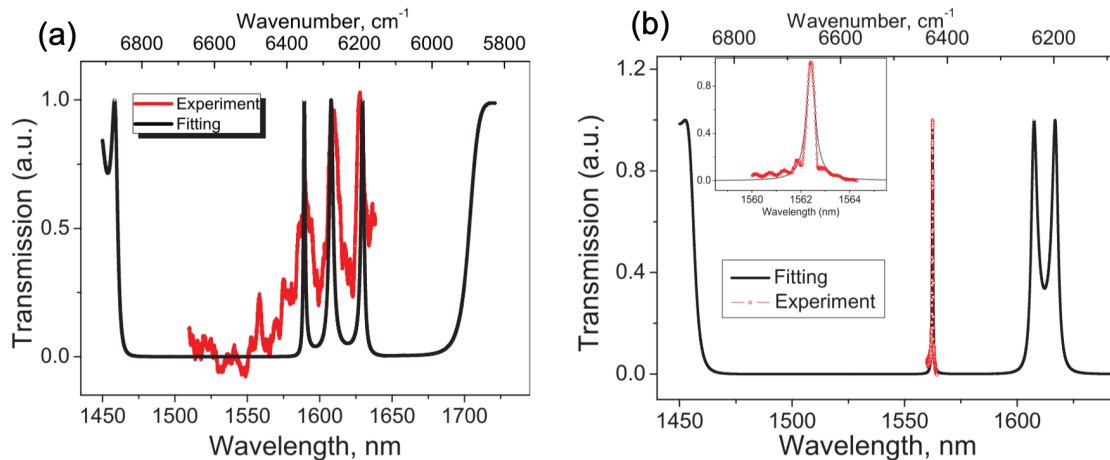

Figure 6. Simulated (black) and experimental (red) transmission spectra of (a) triple resonance system with refractive index of LC filler of $n_c =$1.68 in 2nd, 4th, and 6th grooves and (b) single resonance system realized by application of 10V to the 4th groove and reduction of refractive index to $n_c = 1.458$. A magnified view of the single resonance peak can be found in the inset figure.[51]

2.2 Si-rich nitride graphene capacitor based micro-rings for HPC

We demonstrate the potential of a graphene capacitor structure on silicon-rich nitride micro-ring resonators for multitasking operations within high performance computing (HPC) [Fig. 7]. Capacitor structures formed by two graphene sheets separated by a 10 nm insulating silicon nitride layer are considered. Hybrid integrated photonic structures are then designed to exploit the electro-absorptive operation of the graphene capacitor to tuneably control of the transmission and the attenuation of different wavelengths of light. By tuning the capacitor length, a shift in the resonant wavelength is produced giving rise to a broadband multilevel photonic volatile memory. The advantages of using silicon-rich nitride as the waveguiding material in place of the more conventional silicon nitride ($Si_3 3N_4$) are shown, with a doubling of the device's operational bandwidth from 31.2 to 62.41 GHz achieved while also allowing a smaller device footprint.[53] A difference in the extinction ratio between the ON and OFF states of 16.5 dB and energy consumption of <0.3 pJ/bit are obtained. Finally, it has been demonstrated that increasing the permittivity of the insulator layer in the capacitor structure, the energy consumption per bit can be reduced even further. Overall, the resonance tuning enabled by the novel graphene capacitor makes it a key component for future multilevel photonic memories and optical routing in high performance computing.
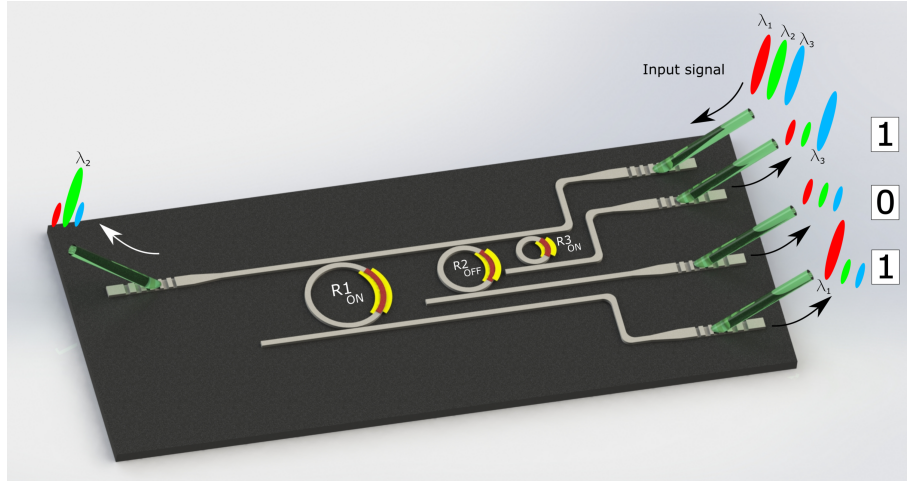
Figure 7. Schematic of a photonic integrated circuit for HPC using as the key component, reconfigurable SRN micro-rings structures based on graphene capacitors for future volatile memories and optical routing.[53]

In order to calculate the speed of the device and the time response, we define an equivalent RC circuit [Fig. 8]. The time response of the RC circuit can be calculated using $V(t) = V_0 e^{-t/\tau}$ where $\tau = RC$ and the speed of the device can be calculated using the response bandwidth, which is determined by:
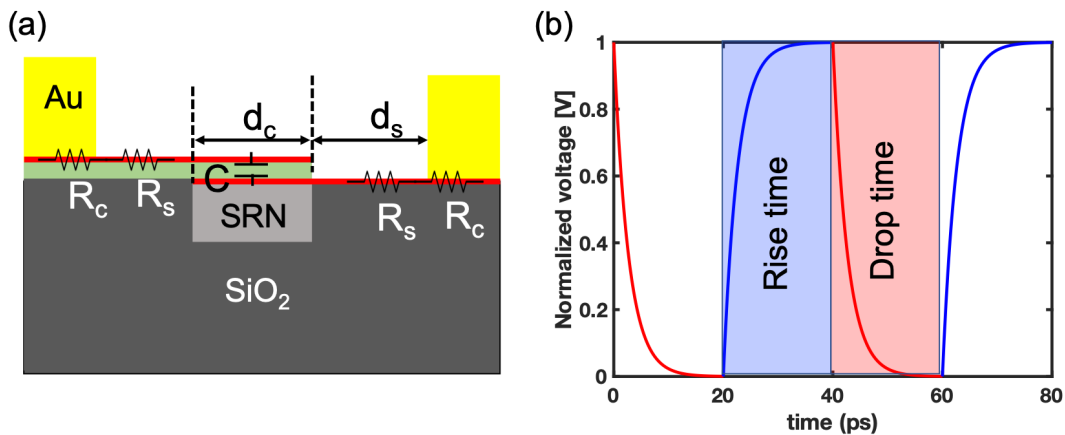
$$Bdw = \frac{1}{2\pi[2(R_c + R_s)] \cdot C} \qquad (3)$$

Figure 8. (a)HWGC cross-section showing the defined equivalent circuit of the graphene capacitor and contacts where R_c, R_s are the contact and the sheet resistance respectively and C is the capacitance. d_c is the graphene capacitor width and d_s is the distance between the contacts and the waveguide. (b) Time response of the HWGC.[53]

where R_c and R_s are the contact and sheet resistances of graphene respectively, and C is the capacitance of the device. The contact resistance of graphene emerges from the Fermi level mismatch between the graphene and the metallic electrodes. This parameter depends on the quality of the graphene and the metal selected for the electrode.[54] Experimental results have previously shown values of the contact resistivity (ρ_c) in the range of

100 to $1000\Omega\mu m$.[55,56] The total contact resistance of graphene is calculated as $R_c = \rho_c/L_g$. In our calculations, we assumed a conservative value of $\rho_C = 1000\Omega\mu m$. The graphene's sheet resistance, is usually defined by the resistance per square, R_{SQ}. The values of R_{SQ} for graphene are typically between 100 and 500 Ω/sq,[57–59] in all of our calculations, we assume a conservative value of 500 Ω/sq. To obtain the total sheet resistance of graphene, we need to consider the contribution of all the squares constituting the device. The total sheet resistance can be expressed as $R_s = R_{SQ} \cdot \frac{d_s}{L_g}$. The width of the graphene capacitor is selected to be d_c=1.2 μm entirely covering the waveguide [Fig. 8]. Using a (Si_3N_4) waveguide, the distance between the gold contacts is selected to be 1 μm to ensure that the metal does not contribute to the losses. A bandwidth response of 12.5 GHz has been calculated in this case. Using SRN as the waveguide material instead of Si_3N_4, the contacts can be closer to the waveguide (400 nm) without affecting the mode propagation [Fig. 9(a)], reducing by 600 nm the distance between the graphene capacitor and the golden contact compared with Si_3N_4. Consequently, R_s is reduced and the calculated device bandwidth increases to 15.6 GHz. For the best case scenario of contact resistance ($\rho_C = 100\Omega\mu m$) maintaining a conservative value in the sheet resistance ($R_{SQ} = 500\Omega/sq$), the bandwidth will increase up to 31.2 GHz and 62.41 GHz for Si_3N_4 and SRN respectively [Fig. 9(b)]. Examining Eq. 3 one can observe that when the capacitance and resistances are multiplied, the length of the device L_g is cancelled out; therefore, the length of the device has no impact on the response bandwidth and only influences the insertion losses (IL). The IL per unit length of our graphene capacitor devices are 0.13 dB/μm and 0.01 dB/μm for the OFF and ON states respectively.
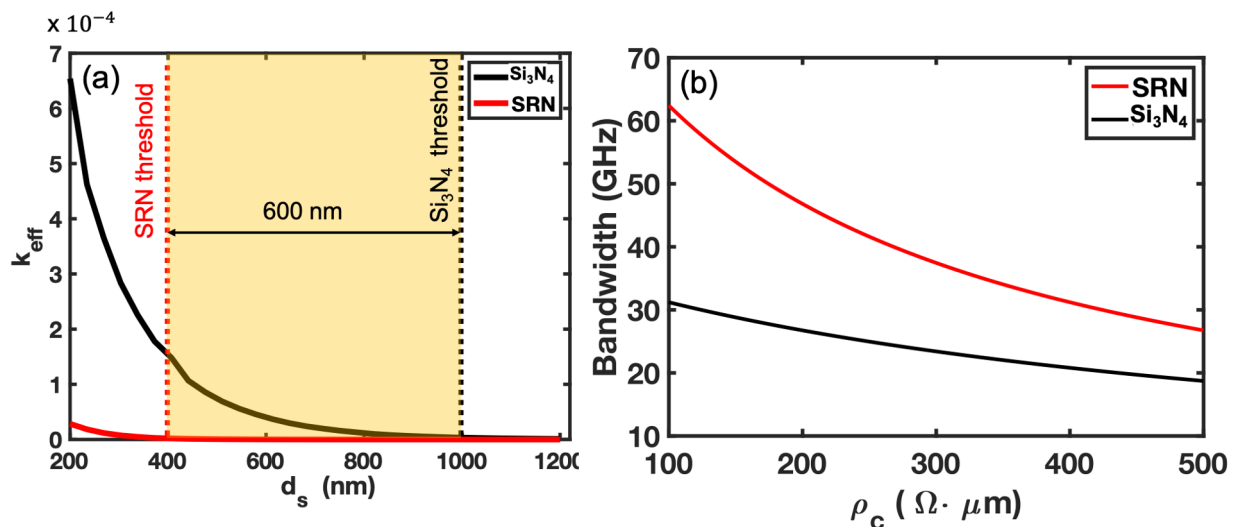

Figure 9. (a) Parametric sweep study of the k_{eff} in the mode against the distance between the contact and the graphene capacitor (d_s) for values between 200-1200 nm for Si_3N_4 (black line) and for Silicon Rich Nitride (SRN) (red line) (b) Parametric sweep study of the contact resistance for Si_3N_4 platform (black line) and for SRN (red line).[53]

2.3 N-rich Silicon Nitride reconfigurable Mach–Zehnder interferometer based on phase change material in the O-band

We have experimentally demonstrated a tuneable O-band N-rich Silicon Nitride Mach-Zehnder interferometer (MZI) based on phase change material for future optical communications applications. The device operation is based on the ON/OFF switching of the waveguide loss with the deposited $Ge_2Sb_2Te_5$ (GST) patch which can change state from amorphous to crystalline. An extinction ratio (ER) as high as 11 dB between the amorphous (ON) and the crystalline (OFF) states of the MZI optical switch is achieved.

The optical platform consists of a 700 nm wide SiNx strip waveguide formed by etching a 600 nm thick SiNx layer[60] [Fig. 10 (a)]. This design allows both single TE and TM mode propagation with theoretically negligible

losses in the O-band. A thin layer (10 nm) of phase-change material (PCM) deposited on top of the waveguide (5 μm lenght and 700 nm width) capped by a second layer of amorphous SiO$_2$. In this work we focussed on the phase-change alloy Ge$_2$Sb$_2$Te$_5$ (GST), due to the well-established fabrication methodology and most importantly, due to thoroughly known contrast optical properties for the two metastable phases: amorphous and crystalline which determine the partial attenuation of the guided modes. Along with the characteristic non-volatile tunability with switching times laying in the nanosecond scale[47],[48] this reconfigurable material provides a suitable platform for stable optical modulation exploiting both, straight waveguides, and Mach-Zehnder interferometers in the O-band, as demonstrated in this work.

The spectral response of the MZIs for a patch length of 5 μm for both: amorphous and crystalline states of the phase change material and $\Delta L=$ 40 μm were characterised [Fig. 10 (b)] using an Agilent 8164B tuneable laser source with a wavelength tuning range between 1260 and 1320 nm. The polarisation of the light was controlled to ensure that only TM modes could propagate through the devices. All MZIs structures were connected to input and output grating couplers consisting of a 10 μm width and 40 μm length with a period of 950 nm tapered down to a single-mode waveguide of 700 nm. The angle of the optical fibres was selected to be 14º to ensure maximum coupling at the wavelength of interest (1,310 μm). The crystallization of the phase change material first occurs during the PCVD deposition of silicon oxide cladding for optimization of the grating couplers when temperatures as high as 350 ºC are reached[61] changing the PCM to its crystalline state.

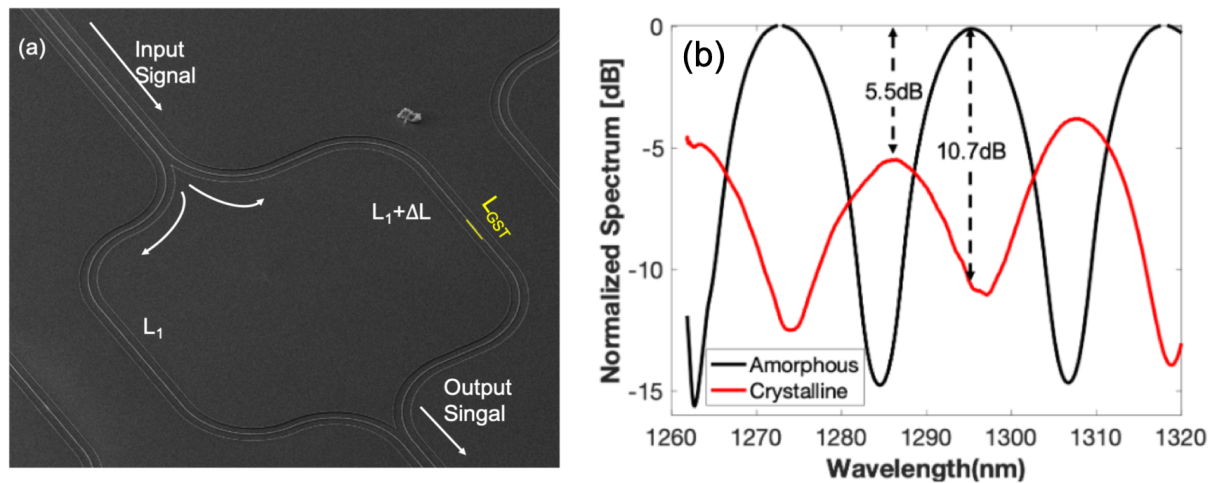
Figure 10. (a) SEM image of a reconfigurable MZI based on phase change material (GST). (b) Transmission for a MZI with $\Delta L=$ 40 μm and $L_{GST}=$ 5 μm in the amorphous state (black line) and in the crystalline state (red line). The spectra are normalized respect to the transmission of the amorphous state.[62]

3. CONCLUSIONS

In this work we have reviewed different functional materials with mature silicon and silicon nitride building blocks to make them tuneable and actively reconfigurable. We have presented a tuneable 1D silicon integrated photonic crystal based on liquid crystals with high quality factor. We have demonstrated the design of faster graphene based optical routing silicon rich micro-ring resonators structures compared with standard silicon nitride, and finally we have experimentally achieved a MZI switch based on phase change materials in the O-band.

ACKNOWLEDGMENTS

REFERENCES

[1] Thomson, D., Zilkie, A., Bowers, J. E., Komljenovic, T., Reed, G. T., Vivien, L., Marris-Morini, D., Cassan, E., Virot, L., Fédéli, J.-M., Hartmann, J.-M., Schmid, J. H., Xu, D.-X., Boeuf, F., O'Brien, P., Mashanovich, G. Z., and Nedeljkovic, M., "Roadmap on silicon photonics," *Journal of Optics* **18**(7), 073003 (2016).

[2] Chrostowski, L. and Hochberg, M., [*Silicon photonics design: from devices to systems*], Cambridge University Press (2015).

[3] Milgram, J. N., Wojcik, J., Mascher, P., and Knights, a. P., "Optically pumped Si nanocrystal emitter integrated with low loss silicon nitride waveguides.," *Optics express* **15**(22), 14679–14688 (2007).

[4] Ikeda, K., Saperstein, R. E., Alic, N., and Fainman, Y., "Thermal and Kerr nonlinear properties of plasma-deposited silicon nitride/ silicon dioxide waveguides," *Optics Express* **16**(17), 12987 (2008).

[5] Bristow, A. D., Rotenberg, N., and Van Driel, H. M., "Two-photon absorption and kerr coefficients of silicon for 850–2200 nm," *Applied Physics Letters* **90**(19), 191104 (2007).

[6] Baets, R., Subramanian, A. Z., Clemmen, S., Kuyken, B., Bienstman, P., Le Thomas, N., Roelkens, G., Van Thourhout, D., Helin, P., and Severi, S., "Silicon photonics: silicon nitride versus silicon-on-insulator," in [*Optical Fiber Communication Conference*], Th3J–1, Optical Society of America (2016).

[7] Lee, M. and Fauchet, P. M., "Two-dimensional silicon photonic crystal based biosensing platform for protein detection," *Optics express* **15**(8), 4530–4535 (2007).

[8] Mishra, A., Basu, A., and Tyagi, V., [*Silicon Photonics & High Performance Computing*], Springer (2018).

[9] Pérez, D., Gasulla, I., Crudgington, L., Thomson, D. J., Khokhar, A. Z., Li, K., Cao, W., Mashanovich, G. Z., and Capmany, J., "Multipurpose silicon photonics signal processor core," *Nature communications* **8**(1), 636 (2017).

[10] Romagnoli, M., Sorianello, V., Midrio, M., Koppens, F. H. L., Huyghebaert, C., Neumaier, D., Galli, P., Templ, W., D'Errico, A., and Ferrari, A. C., "Graphene-based integrated photonics for next-generation datacom and telecom," *Nature Reviews Materials* **3**(10), 392–414 (2018).

[11] Dalir, H., Xia, Y., Wang, Y., and Zhang, X., "Athermal Broadband Graphene Optical Modulator with 35 GHz Speed," *ACS Photonics* **3**(9), 1564–1568 (2016).

[12] Rodríguez-Fortuño, F. J., Espinosa-Soria, A., and Martínez, A., "Exploiting metamaterials, plasmonics and nanoantennas concepts in silicon photonics," *Journal of Optics* **18**(12), 123001 (2016).

[13] Liu, M., Yin, X., Wang, F., and Zhang, X., "Graphene optical modulator," *SPIE Optics 2011* **8101**, 81010J–81010J–6 (2011).

[14] Liu, M., Yin, X., and Zhang, X., "Double-layer graphene optical modulator," *Nano Letters* **12**(3), 1482–1485 (2012).

[15] Mohsin, M., Neumaier, D., Schall, D., Otto, M., Matheisen, C., Lena Giesecke, A., Sagade, A. A., and Kurz, H., "Experimental verification of electro-refractive phase modulation in graphene," *Scientific Reports* **5**, 1–7 (2015).

[16] Thomson, D. J., Gardes, F. Y., Fedeli, J. M., Zlatanovic, S., Hu, Y., Kuo, B. P. P., Myslivets, E., Alic, N., Radic, S., Mashanovich, G. Z., and Reed, G. T., "50-Gb/s silicon optical modulator," *IEEE Photonics Technology Letters* **24**(4), 234–236 (2012).

[17] Romagnoli, M., "Graphene photonics for optical communications," in [*Optical Fiber Communication Conference*], M3D–3, Optical Society of America (2019).

[18] Jalali Azizpour, M. R., Soroosh, M., Dalvand, N., and Seifi-Kavian, Y., "All-optical ultra-fast graphene-photonic crystal switch," *Crystals* **9**(9), 461 (2019).

[19] Faneca, J., Hogan, B. T., Diez, I. R., Gardes, F. Y., and Baldycheva, A., "Tuning silicon-rich nitride microring resonances with graphene capacitors for high-performance computing applications," *Opt. Express* **27**, 35129–35140 (Nov 2019).

[20] Gardes, F., Reed, G., Emerson, N., and Png, C., "A sub-micron depletion-type photonic modulator in silicon on insulator," *Optics Express* **13**(22), 8845–8854 (2005).

[21] Ríos, C., Stegmaier, M., Hosseini, P., Wang, D., Scherer, T., Wright, C. D., Bhaskaran, H., and Pernice, W. H. P., "Integrated all-photonic non-volatile multi-level memory," *Nature Photonics* **9**(11), 725–732 (2015).

[22] Reed, G. T., Mashanovich, G., Gardes, F. Y., and Thomson, D., "Silicon optical modulators," *Nature photonics* **4**(8), 518 (2010).

[23] Wang, S., Kawakami, Y., Simpson, J., Stewart, H., Prior, K., and Cavenett, B., "Znse-zncdse quantum confined stark effect modulators," *Applied physics letters* **62**(15), 1715–1717 (1993).

[24] Welstand, R., Sun, C., Pappert, S., Liu, Y., Chen, J., Zhu, J., Kellner, A., and Yu, P., "Enhanced linear dynamic range property of franz-keldysh effect waveguide modulator," *IEEE photonics technology letters* **7**(7), 751–753 (1995).

[25] Andrienko, D., "Introduction to liquid crystals," *Journal of Molecular Liquids* **267**, 520–541 (2018).

[26] Yu, S., Wu, X., Wang, Y., Guo, X., and Tong, L., "2D Materials for Optical Modulation: Challenges and Opportunities," *Advanced Materials* **29**(14) (2017).

[27] Jeon, S., Jia, J., Ju, J. H., and Lee, S., "Black phosphorus photodetector integrated with au nanoparticles," *Applied Physics Letters* **115**(18), 183102 (2019).

[28] Bie, Y.-Q., Grosso, G., Heuck, M., Furchi, M. M., Cao, Y., Zheng, J., Bunandar, D., Navarro-Moratalla, E., Zhou, L., Efetov, D. K., et al., "A mote 2-based light-emitting diode and photodetector for silicon photonic integrated circuits," *Nature nanotechnology* **12**(12), 1124 (2017).

[29] Fryett, T. K., Seyler, K. L., Zheng, J., Liu, C.-H., Xu, X., and Majumdar, A., "Silicon photonic crystal cavity enhanced second-harmonic generation from monolayer wse2," *2D Materials* **4**(1), 015031 (2016).

[30] Youngblood, N. and Li, M., "Integration of 2d materials on a silicon photonics platform for optoelectronics applications," *Nanophotonics* **6**(6), 1205 (2017).

[31] Shiue, R.-J., Gao, Y., Wang, Y., Peng, C., Robertson, A. D., Efetov, D. K., Assefa, S., Koppens, F. H., Hone, J., and Englund, D., "High-responsivity graphene–boron nitride photodetector and autocorrelator in a silicon photonic integrated circuit," *Nano letters* **15**(11), 7288–7293 (2015).

[32] Wolf, E. L., [*Applications of Graphene: An Overview (SpringerBriefs in Materials)*] (2014).

[33] Ricardo A Depine, [*Graphene Optics*].

[34] Wang, F., Zhang, Y., Tian, C., Girit, C., Zettl, A., Crommie, M., and Shen, Y. R., "Gate-Variable Optical Transitions in Graphene," *Science* **320**(5873), 206–209 (2008).

[35] Chen, C.-F., Park, C.-H., Boudouris, B. W., Horng, J., Geng, B., Girit, C., Zettl, A., Crommie, M. F., Segalman, R. A., Louie, S. G., and Wang, F., "Controlling inelastic light scattering quantum pathways in graphene," *Nature* **471**(7340), 617–620 (2011).

[36] Sundaram, R. S., Engel, M., Lombardo, A., Krupke, R., Ferrari, A. C., Avouris, P., and Steiner, M., "Electroluminescence in single layer MoS2," *Nano Letters* **13**(4), 1416–1421 (2013).

[37] Yang, W., Kawai, H., Bosman, M., Tang, B., Chai, J., Le Tay, W., Yang, J., Seng, H. L., Zhu, H., Gong, H., et al., "Interlayer interactions in 2d ws 2/mos 2 heterostructures monolithically grown by in situ physical vapor deposition," *Nanoscale* **10**(48), 22927–22936 (2018).

[38] Sun, Z., Martinez, A., and Wang, F., "Optical modulators with 2d layered materials," *Nature Photonics* **10**(4), 227 (2016).

[39] Buller, S., Koch, C., Bensch, W., Zalden, P., Sittner, R., Kremers, S., Wuttig, M., Schurmann, U., Kienle, L., Leichtweiß, T., et al., "Influence of partial substitution of te by se and ge by sn on the properties of the blu-ray phase-change material ge8sb2te11," *Chemistry of Materials* **24**(18), 3582–3590 (2012).

[40] Peng, K., Chen, C., Pan, W., Liu, W., Wang, Z., and Zhu, L., "Preparation and properties of β-cyclodextrin/4, 4-diphenylmethane diisocyanate/polyethylene glycol (β-cd/mdi/peg) crosslinking copolymers as polymeric solid–solid phase change materials," *Solar Energy Materials and Solar Cells* **145**, 238–247 (2016).

[41] Atwood, G., "Phase-change materials for electronic memories," *Science* **321**(5886), 210–211 (2008).

[42] Pirovano, A., Lacaita, A. L., Benvenuti, A., Pellizzer, F., and Bez, R., "Electronic switching in phase-change memories," *IEEE Transactions on Electron Devices* **51**(3), 452–459 (2004).

[43] Lai, S., "Current status of the phase change memory and its future," in [*IEEE International Electron Devices Meeting 2003*], 10–1, IEEE (2003).

[44] El-Hinnawy, N., Borodulin, P., Wagner, B., King, M. R., Mason, J. S., Jones, E. B., McLaughlin, S., Veliadis, V., Snook, M., Sherwin, M. E., et al., "A four-terminal, inline, chalcogenide phase-change rf switch using an independent resistive heater for thermal actuation," *IEEE Electron Device Letters* **34**(10), 1313–1315 (2013).

[45] Rios, C., Hosseini, P., Wright, C. D., Bhaskaran, H., and Pernice, W. H. P., "On-chip photonic memory elements employing phase-change materials," *Advanced Materials* **26**(9), 1372–1377 (2014).

[46] Farmakidis, N., Youngblood, N., Li, X., Tan, J., Swett, J. L., Cheng, Z., Wright, C. D., Pernice, W. H., and Bhaskaran, H., "Plasmonic nanogap enhanced phase-change devices with dual electrical-optical functionality," *Science Advances* **5**(11), eaaw2687 (2019).

[47] Hegedüs, J. and Elliott, S. R., "Microscopic origin of the fast crystallization ability of Ge-Sb-Te phase-change memorymaterials," *Nature Materials* **7**(5), 399–405 (2008).

[48] Matsunaga, T. and Yamada, N., "A study of highly symmetrical crystal structures, commonly seen in high-speed phase-change materials, using synchrotron radiation," *Japanese Journal of Applied Physics, Part 1: Regular Papers and Short Notes and Review Papers* **41**(3 B), 1674–1678 (2002).

[49] Wełnic, W., Botti, S., Reining, L., and Wuttig, M., "Origin of the optical contrast in phase-change materials," *Physical Review Letters* **98**(23), 1–4 (2007).

[50] Zheludev, N. I. and Kivshar, Y. S., "From metamaterials to metadevices," *Nature Materials* **11**(11), 917–924 (2012).

[51] Faneca, J., Perova, T. S., Tolmachev, V., and Baldycheva, A., "One-dimensional multi-channel photonic crystal resonators based on silicon-on-insulator with high quality factor," *Frontiers in Physics* **6**, 33 (2018).

[52] Faneca, J., Perova, T. S., Tolmachev, V., and Baldycheva, A., "One-Dimensional Multi-Channel Photonic Crystal Resonators Based on Silicon-On-Insulator With High Quality Factor," *Frontiers in Physics* **6**(May), 1–9 (2018).

[53] Faneca, J., Hogan, B. T., Diez, I. R., Gardes, F. Y., and Baldycheva, A., "Tuning silicon-rich nitride microring resonances with graphene capacitors for high-performance computing applications," *Optics Express* **27**(24), 35129–35140 (2019).

[54] Kovacevic, G., Phare, C., Set, S. Y., Lipson, M., and Yamashita, S., "Ultra-high-speed graphene optical modulator design based on tight field confinement in a slot waveguide," *Applied Physics Express* **11**(6) (2018).

[55] Venugopal, A., Colombo, L., and Vogel, E. M., "Contact resistance in few and multilayer graphene devices," *Applied Physics Letters* **96**(1) (2010).

[56] Leong, W. S., Luo, X., Li, Y., Khoo, K. H., Quek, S. Y., and Thong, J. T., "Low resistance metal contacts to MoS 2 devices with nickel-etched-graphene electrodes," *ACS Nano* **9**(1), 869–877 (2015).

[57] Sorianello, V., Midrio, M., and Romagnoli, M., "Design optimization of single and double layer Graphene phase modulators in SOI," *Optics Express* **23**(5), 6478 (2015).

[58] Lee, J. K., Park, C. S., and Kim, H., "Sheet resistance variation of graphene grown on annealed and mechanically polished Cu films," *RSC Advances* **4**(107), 62453–62456 (2014).

[59] Ishikawa, R., Kurokawa, Y., Miyajima, S., and Konagai, M., "Peeling process of thin-film solar cells using graphene layers," *Applied Physics Express* **10**(8) (2017).

[60] Bucio, T. D., Khokhar, A. Z., Mashanovich, G. Z., and Gardes, F. Y., "N-rich silicon nitride angled MMI for coarse wavelength division (de)multiplexing in the O-band," *Optics Letters* **43**(6), 1251 (2018).

[61] Friedrich, I., Weidenhof, V., Njoroge, W., Franz, P., and Wuttig, M., "Structural transformations of Ge2Sb2Te5 films studied by electrical resistance measurements," *Journal of Applied Physics* **87**(9), 4130–4134 (2000).

[62] Bucio, T. D., Lacava, C., Clementi, M., Faneca, J., Skandalos, I., Baldycheva, A., Galli, M., Debnath, K., Petropoulos, P., and Gardes, F., "Silicon nitride photonics for the near-infrared," *IEEE Journal of Selected Topics in Quantum Electronics* **26**(2), 1–13 (2019).